Article

Active hydraulics laws from frustration principles

Camille Jorge ⓘ[1], Amélie Chardac ⓘ[1,2], Alexis Poncet ⓘ[1] & Denis Bartolo ⓘ[1]✉

Viscous flows are laminar and deterministic. Robust linear laws accurately predict their streamlines in geometries as complex as blood vessels, porous media and pipe networks. However, biological and synthetic active fluids defy these fundamental laws. Irrespective of their microscopic origin, confined active flows are intrinsically bistable, making it challenging to predict flows in active fluid networks. Although early theories attempted to tackle this problem, quantitative experiments to validate their relevance to active hydraulics are lacking. Here we present a series of laws that accurately predict the geometry of active flows in trivalent networks. Experiments with colloidal rollers reveal that active hydraulic flows realize dynamical spin ices: they are frustrated, non-deterministic and yield degenerate streamline patterns. These patterns split into two geometric classes of self-similar loops, which reflect the fractionalization of topological defects at subchannel scales. Informed by our measurements, we formulate the laws of active hydraulics in trivalent networks as a double-spin model. We then use these laws to predict the random geometry of degenerate streamlines. We expect our fundamental understanding to provide robust design rules for active microfluidic devices and to offer avenues to investigate the motion of living cells and organisms in complex habitats.

When they invented irrigation, the ancient civilizations of Egypt and Mesopotamia relied on the first fundamental rule of hydraulics: mass conservation[1]. In our modern language, we formulate it as Kirchhoff's first law. In the steady state, the sum of fluxes must vanish at each node of a channel network ($\sum_j \Phi_{ij} = 0$, where Φ_{ij} is the flux from node j to node i). Eight millennia later, Hagen, Poiseuille and Darcy discovered the second law of hydraulics[2–4]. Darcy's law relates the mass fluxes to pressure gradients: $\Phi_{ij} = -K_{ij}(P_i - P_j)$, where P_i is the fluid pressure and K_{ij} is the hydraulic conductance. Given these two linear relations and a set of boundary conditions, we can predict the viscous flows in any hydraulic network, regardless of their geometrical complexity. Although it can be computationally hard to solve and optimize, viscous hydraulics are deterministic and fully predictable.

However, over the past decade, physicists, chemists and material scientists have complexified this neat picture. They have engineered active fluids that escape the fundamental laws of hydraulics[5]. Either by hacking biological engines (such as molecular motors and bacteria) or by motorizing synthetic soft materials, we have learned how to power fluids at the scale of their elementary building blocks. When confined, the resulting active materials enjoy spontaneous laminar flows even in the absence of any external drive or boundary motion[6–12]. In channels and pipes, active fluids flow in one direction or the other with the same probability, and can even resist opposing pressure gradients[13]. In other words, they are intrinsically bistable[9,13,14]. This fundamental deviation from Darcy's law makes active hydraulics a challenging problem. From a theoretical perspective, the fundamental multistability of active hydraulic flows was realized and the computational power of active fluidic networks (AFNs) based on minimal models was investigated[14–17]. From an experimental perspective, the investigation of active hydraulics has been mostly limited to straight channel geometries, closed loops and one-node networks[7,9,18]. Today, the basic laws of active hydraulics remain to

[1]Univ. Lyon, ENS de Lyon, Univ. Claude Bernard, CNRS, Laboratoire de Physique, Lyon, France. [2]Department of Physics, Brandeis University, Waltham, MA, USA. ✉e-mail: denis.bartolo@ens-lyon.fr
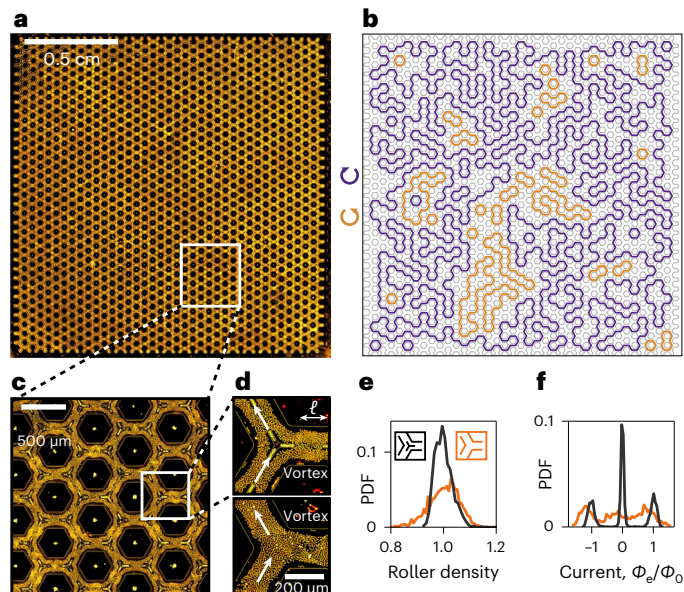
Fig. 1 | Active hydraulics in trivalent networks. a, Macroscopic picture of a trivalent microfluidic network. It encloses a two-dimensional active fluid made of flocking Quincke rollers. **b**, Experimental streamlines measured in this active hydraulic network. The streamlines form self-avoiding loops coloured by their handedness. **c**, Close-up view of the experimental device. We can distinguish steady vortices in a finite fraction of the channels. **d**, Our results do not depend on the specific geometry of the nodes that connect the microfluidic channels. A node including a star-shaped flow splitter (top). A node with no splitter (bottom). In the steady state, only two of the three channels support laminar flows. The third (horizontal) channel hosts a steady vortex. **e**, Distribution of the roller density normalized by the average density in the channels. The density is homogeneous in all the experiments, but features fewer fluctuations when the nodes include a star-shaped splitter. **f**, Distribution of local edge current Φ_e normalized by $\Phi_0 = 400$ s^{-1}. The distribution is trimodal for both node geometries (the sign convention used to define Φ_e is sketched and explained in Fig. 2a). PDF, probability distribution function.

be experimentally tested, confirmed or established, in large-scale networks.

In this Article, we perform large-scale active hydraulics experiments. We show that spontaneous laminar flows are frustrated in networks including nodes with an odd coordination number. Focusing on fully frustrated trivalent networks, we show that the resulting active flows realize dynamical spin ices signalled by extensively degenerate random flow patterns even when the channels are spatially ordered. Unlike passive fluids, and at odds with the current AFN theory, we find that the random geometry of streamlines depends on the aspect ratio of the elementary channels. We explain this polymorphism by combining experiments and numerical simulations, and show that it originates from topological-defect fractionalization at the subchannel level. We then elucidate the self-similar geometry of the flow patterns by mapping them on the frustrated structures of magnetic spin ices and on so-called loop $O(n)$ models[19–22]. Altogether, our findings allow us to identify the full set of laws ruling the steady flows of active matter circulating through interconnected channels forming trivalent networks.

To experimentally investigate active hydraulics, we need a model active fluid and model hydraulic networks (Fig. 1). Methods provides all the technical details. In short, our active fluid is a flocking liquid assembled from Quincke rollers[6], which features bistable laminar flows in straight channels[13]. We first confine our active fluid in networks of channels that form a honeycomb structure including up to 3,200 trivalent nodes (Fig. 1a,b). In their early experiments, Wioland et al. showed

that active flows can strongly depend on the specific geometry of their boundaries[23]. We, therefore, consider two different node geometries where the trivalent junctions either include a star-shaped splitter or not (Fig. 1d). We also systematically vary the aspect ratio $\epsilon = w/\ell$ of the roller streams in the channels, by varying their length ℓ from 120 to 220 μm (Fig. 1d). The channel width w is kept constant and equal to 200.0 μm, about a hundred times larger than the colloids' radius (2.4 μm).

We first observe a transient dynamics where the active fluid undergoes strong density and velocity fluctuations over system-spanning scales (Supplementary Video 1). The convergence towards a stable steady state depends on the initial fluctuations in the colloid density and on the system size. However, in typically less than a couple of minutes, we found that the active flows converge towards a quiet steady state where the streamlines form a soup of self-avoiding loops (Fig. 1b). The quantitative characterization and prediction of these random streamline patterns from basic laws is our essential result. We also note that the density of the active fluid is homogeneous across the whole device (Fig. 1e and Supplementary Videos 2 and 3). By contrast, the mass–current distribution in the channels is heterogeneous (Fig. 1f). It is trimodal with two symmetric peaks associated with spontaneous flows at constant speed, and one higher peak that reveals channels with no net current. Although the statistics of the flow pattern remain qualitatively unchanged, we find that the peaks of the density and current distributions are narrower when using the splitter geometry (Fig. 1d). All the results reported below, therefore, correspond to this node geometry. Performing a series of experiments in deformed lattice geometries (Extended Data Fig. 1), we also checked that our results are solely determined by valence of the nodes and not by the C_3 symmetry typical of a honeycomb structure (Fig. 1).

Unlike in disconnected straight channels, the active flows are never laminar throughout the sample: at least 40% of the channels host steady vortices and therefore support no net mass flux (Fig. 1d,f). This series of observations stems from the geometrical frustration of active laminar flows in trivalent networks[14,17]. It can be understood as follows. As in most active fluids, the spontaneous flows of the Quincke rollers operate at constant speed. When the fluid density is homogeneous, the magnitude of the net fluxes $|\Phi_e|$ measured along all the network edges (e) peaks on a constant value Φ_0. The sign of Φ_e is defined in Fig. 2a. In our experiments, $\Phi_0 = 400$ s^{-1} (Fig. 1e). The active flows are, therefore, frustrated at any node with an odd coordination number. Flowing at constant speed and conserving mass are two incompatible constraints that cannot be simultaneously met in the steady state. Each node accommodates frustration owing to the emergence of vortices in one edge where the flux vanishes ($\Phi_e = 0$) (Fig. 2b and Supplementary Videos 4 and 5). Irrespective of the channel aspect ratio, the situation where all three fluxes vanish is also possible, yet less probable (Extended Data Fig. 2 and Supplementary Video 6).

The geometry of the streamlines must, therefore, accommodate the conflicting imperatives set by activity and mass conservation. The resulting local frustration defines a set of seven possible flow rules at the vertices, which are classified in Fig. 2c. From a condensed-matter perspective, they are akin to the spin-ice rules responsible for the ground-state degeneracy of magnetic textures in frustrated magnets[19–22]. More specifically, the six-most probable vertices (Fig. 2c) define a three-colouring model on the honeycomb lattice[24,25], as evident in Fig. 2b. This first analogy with spin-ice physics explains the vast degeneracy of the flow patterns found in our experiments. Active hydraulic flows are not deterministic. Repeating the same experiment in the same periodic geometry, we observe a plethora of disordered flow patterns. We illustrate them in Fig. 2d and their overlap distribution shows that they hardly feature any correlation (Fig. 2e).

The streamlines form nearly close-packed ensembles of self-avoiding loops. This geometry is a direct consequence of the spin-ice rules (Fig. 2c), where the seven vertices are the generators of the self-avoiding random loops on the honeycomb lattice. Consistently,
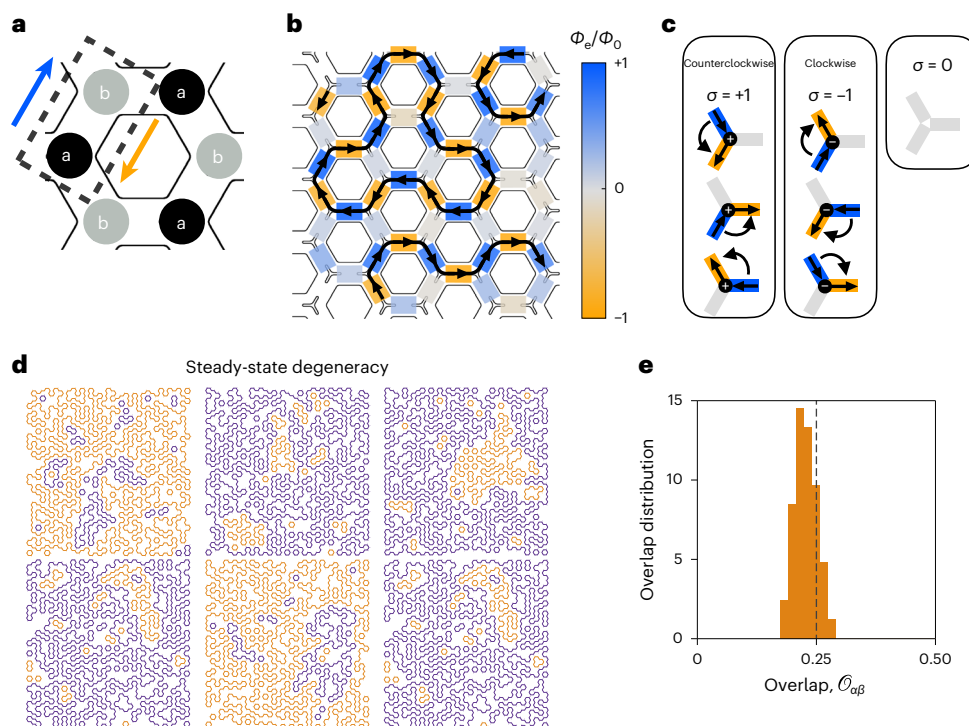
Fig. 2 | Degeneracy of the streamline patterns. a, Sign convention of edge current Φ_e. The honeycomb lattice is bipartite. Its unit cell includes two sites, say 'a' and 'b'. Φ_e is defined to be positive (blue arrow) when the active fluid flows from the a site to the b site and negative otherwise (orange arrow). **b**, Heat map showing the local value of current Φ_e. The solid lines indicate the shape of the corresponding streamlines. The data correspond to the region of space shown in Fig. 1c. **c**, Classification of the seven possible vertices at each node. The colours indicate the sign of the current. Φ_e is associated to a classical spin-1 variable, namely, $\Phi_e \in \{-1, +1, 0\}$ (negative, positive and vanishing net current, respectively). We define another spin variable $\sigma \in \{-1, 0, 1\}$ at the nodes of the network. σ represents the handedness of the three-colour patterns. **d**, Six realizations of the same experiment ($\epsilon = 0.7$) lead to six different streamline patterns with markedly different geometries. The colour indicates the

handedness of the oriented loops. **e**, Overlap distribution computed over ten independent replicas of the same experiment indicates very little correlations from one replica to another. $\mathcal{O}_{\alpha\beta} = \langle 1 - |\Phi_\alpha(e) - \Phi_\beta(e)| \rangle_e$ quantifies the difference between the flow patterns in replicas α and β (Methods). The typical overlap is 0.2, which is consistent with the value expected for uncorrelated random current fields ($\langle \mathcal{O}_e^{\alpha\beta} \rangle \in [0.16 - 0.25]$). In the limit case where $\Phi_\alpha(e)$ are uncorrelated, we can perform a crude approximation. Ignoring spatial correlations, we define the probability $(1 - 2p)$ such that $\Phi(e) = 0$ and assume that $\Phi(e) = \pm 1$ have the same probability p. The average overlap between two random configurations would then be $\langle \mathcal{O}_e^{\alpha\beta} \rangle = 1 - 4p(1 - p)$. Estimating p from the fraction of edges supporting no net current, we find $p \in [0.25 - 0.30]$, which yields $\langle \mathcal{O}_e^{\alpha\beta} \rangle \in [0.16 - 0.25]$.

self-avoiding patterns were already numerically observed in AFN models[15] for degree-3-vertex graphs where the flow rules essentially reduce to that shown in Fig. 2c. However the loops' morphology strongly depends on the aspect ratio of the channels, ϵ (Fig. 3a). Obviously, this polymorphism cannot be explained by the sole spin-ice rule shown in Fig. 2c as it is agnostic to the channel lengths. To explain this, we first quantitatively characterize the loops' geometry. We find that for all channel aspect ratios, the loops are self-similar: their gyration radius R_g grows algebraically with their length L as $R_g \propto L^\nu$ (Fig. 3b). Moreover, for small ϵ values, the loops are collapsed and segregated; by contrast, when ϵ is large, the streamlines are more persistent and form nested structures. We quantify these observations by plotting the exponent of gyration radius ν. We find that it undergoes a sharp increase when ϵ exceeds $\epsilon^* = 0.8$ (Fig. 3c).

The transition from segregated to nested loops occurs at the same value of ϵ^*. To see this, we classically identify the oriented streamlines with the contour lines of the height fields h of rough landscapes[26]. Figure 3a shows the topographic maps h corresponding to two streamline patterns (Methods). We then quantify the level of nesting by the maximum height difference Δh, which increases sharply at ϵ^* (Fig. 3b).

These observations prompt us to deeply investigate the orientational interactions between the streamlines. To do so, we measure the fraction of parallel configurations when two adjacent streamlines are separated by a channel supporting no net flux (Fig. 4b). To measure this

quantity, we note that it is given by $\langle 1 + \sigma_1 \sigma_2 \rangle / 2$ where spin variables σ_i measure the handedness of the vertices (Figs. 2c and 4a).

Figure 4b shows that antiparallel contacts ($\sigma_1 \sigma_2 = -1$) prevail when $\epsilon < \epsilon^*$, whereas most of the contacts are parallel ($\sigma_1 \sigma_2 = +1$) when $\epsilon > \epsilon^*$. This central result indicates that active hydraulic flows are not only shaped by the spin-ice rules but also by short-range orientational interactions between adjacent streamlines. To elucidate their nature, we investigate the morphology of the vortical flows at the subchannel scale (Fig. 4a). We find a clear structural change at ϵ^*. Below ϵ^*, the channels with no net flux ($\Phi_e = 0$) host a single vortex. This vortex couples the adjacent channels as a gear would couple two circulators. The continuity of the flow field then favours antiparallel couplings between neighbouring streamlines. This short-range coupling is consistent with collapsed streamline loops including a number of hairpins (Fig. 4e).

The situation for $\epsilon > \epsilon^*$ is more subtle. We find that the zero-flux channels host two vortices (Fig. 4a). In most channels, they rotate in opposite directions (Fig. 4b). The continuity of the flow field, therefore, promotes parallel couplings, which explains the emergence of a nested structure of streamlines, as evident in Fig. 4f. However, in Fig. 4a, we can also see configurations with two co-rotating vortices, which promote antiparallel couplings. We now need to understand whether the dominance of counter-rotating vortices is specific to our experiments or generic to polar active fluids. We address this question numerically. We model the active flows using Toner–Tu hydrodynamics of polar active matter[27,28], and solve these generic equations using a finite-element
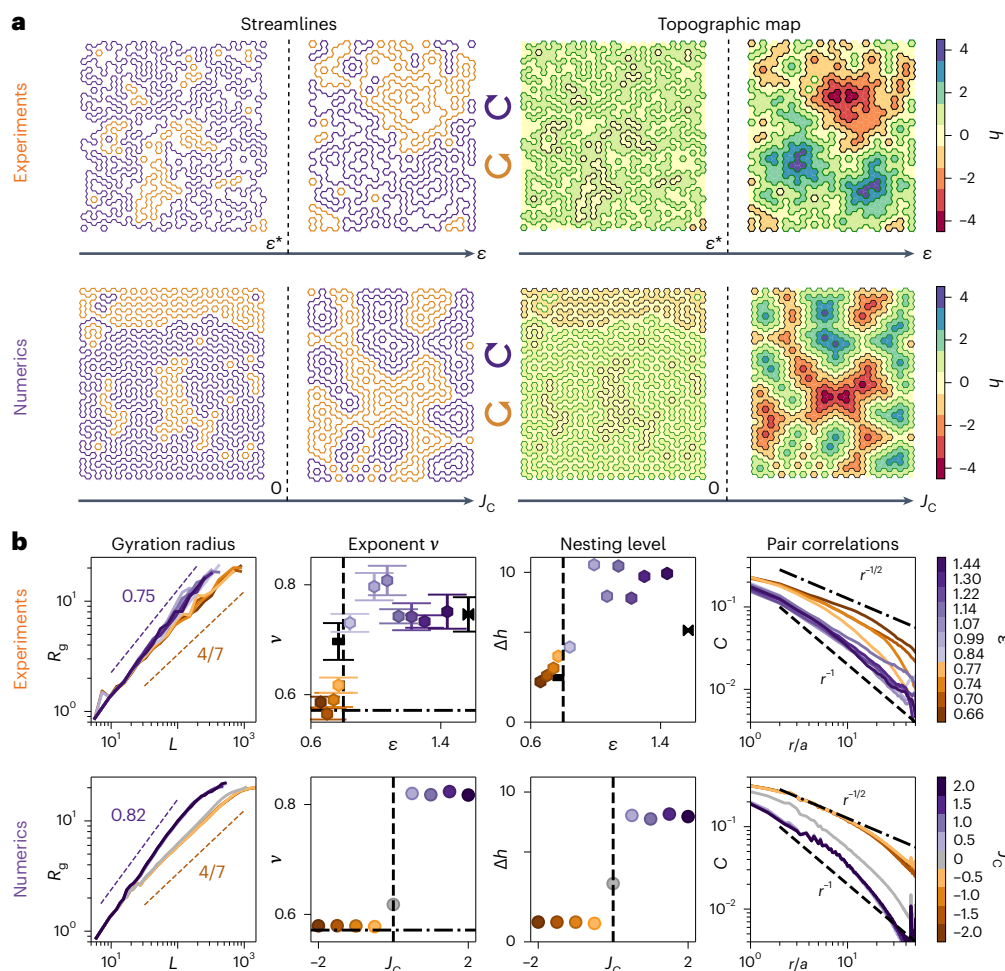
Fig. 3 | Polymorphism of streamlines. a, Evolution of the streamline morphology. The top row shows the data from the experiments. Two sets of streamlines correspond to $\epsilon = 0.7$ and $\epsilon = 1.1$ (left). Below $\epsilon^* = 0.8$, they are crumpled and segregated. Above ϵ^*, they are nested and persistent. Corresponding topographic maps (right) (Methods). Below ϵ^*, the segregation of streamlines translates in a two-level topography. Above ϵ^*, the map features high hills and deep valleys. The bottom row shows data from the numerical simulations. Streamlines and topographic maps are predicted by the equilibrium configurations of the Hamiltonian defined by equation (1) for $J_C = -2$ and $J_C = +2$. The qualitative agreement between the simulations and experiments confirms the relevance of our active hydraulics laws. J_C is a good proxy for the channel aspect ratio. **b**, Characterization of the streamline geometries: experiments, simulations and theory. All the simulations are performed on a honeycomb graph having the same size and boundary conditions as in the experiments. In the first column, for all the values of ϵ (experiments) and J_C (simulations), R_g grows algebraically with the length of the streamlines L: $R_g \approx {}^\nu$. The orange dashed lines indicate the theoretical predictions based on the loop $O(1)$ model (Supplementary Information). The second column shows the variations in ν

with aspect ratio ϵ (experiments) and J_C (simulations). The orange hexagons indicate the honeycomb lattices. The dark rectangle and bow-tie symbol indicate the experiments performed in the brick and deformed honeycomb lattices (Supplementary Fig. 1). The dash–dotted line shows the exact prediction in the small J_C and large J_A limit (closely packed loop $O(1)$ model). As per the dashed line, when $J_C = 0$ and $J_A \gg 1$ limit (closely packed loop $O(2)$ model), our experiments and numerical data are consistent with the theoretical prediction $\nu = 2/3$. The third column shows the nesting level quantified by the maximum height difference on the topographic maps (average over ten realizations). The nesting level jumps at $\epsilon = \epsilon^*$ (experiments) and $J_C = 0$ (simulations). The fourth column shows $C(r)$, the probability of finding two nodes at distance r within the same loop. When $\epsilon > \epsilon^*$, this pair correlation decays much faster than when $\epsilon < \epsilon^*$. In the simulations, the plots clearly collapse on two distinct master curves when $J_C \neq 0$. The dash–dotted line shows the exact prediction in the limit $J_C \ll 0$ and the dashed line, the exact prediction for $J_C = 0$. Each experiment has been repeated ten times. The error bars correspond to the 95% confidence interval. Each simulation has been repeated 50 times.

solver (Methods). We consider the simple geometry of an anisotropic cigar-shaped chamber with tangent boundary conditions (Fig. 4c). A systematic investigation would go beyond the scope of this Article; therefore, we focus on a single set of material parameters consistent with earlier measurements in Quincke roller fluids[29,30]. As the channel aspect ratio increases, we observe a clear transition between one-vortex and two-vortex configurations. The velocity field around a point vortex hosts a topological charge of +1. Therefore, when two point vortices coexist, an additional stagnation point of charge −1 must emerge to conserve the overall topological charge of +1 (ref. 30). Remarkably, we find that the most probable configuration does not correspond to

the coexistence of +1 and −1 charges (Fig. 4d). By contrast, we observe a fractionalization of the −1 charge into two singularities of −1/2 (Fig. 4c). The fractional charges corresponding to stagnation points are bound to the channel walls and stabilize the counter-rotation of the two vortices of +1. This numerical result is in excellent agreement with our experimental findings (Fig. 4a). We, therefore, conclude that the prevalence of ferromagnetic couplings between the macroscopic streamlines (Fig. 4b) originates from defect fractionalization in the flow field at the subchannel scale. This consistent observation does not rely on the specifics of Quincke roller experiments.
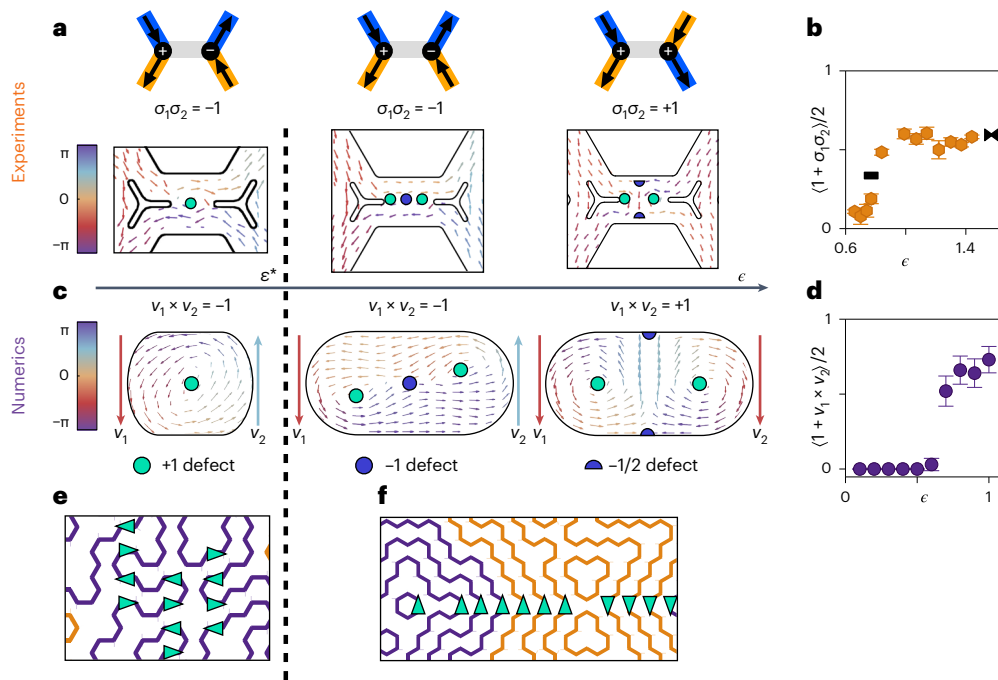
Fig. 4 | Orientational interactions between adjacent streamlines and topological-defect fractionalization. a, Close-up view of the flow field in two adjacent streamlines separated by a channel that supports no net flux. Below ϵ^*, the central channel hosts a single vortex. Above ϵ^*, the central channel hosts two vortices. When two vortices rotate in the same direction, the flow field includes one topological charge of −1 and two charges of +1. When the two vortices rotate in opposite directions, the −1 charge is fractionalized into two −1/2 defects bound to the channel walls. **b**, Fraction of parallel contacts across the channels supporting no net flow. The fraction of parallel contacts is given by $\frac{1}{2}(1 + \sigma_1\sigma_2)$. The orange hexagons indicate honeycomb lattices. The dark rectangles and bow-tie symbols indicate experiments performed in the brick and deformed honeycomb lattices, respectively (Supplementary Fig. 1). The flow couplings are mostly antiparallel below ϵ^* and mostly parallel above. Each experiment has been repeated ten times. **c**, Numerical resolution of the Toner–Tu equations in cigar-shaped boxes (Supplementary Information). We define the aspect ratio of

the boxes as $\epsilon = \ell/w$, where w is the width of the simulation box and ℓ is the length of the straight line joining the half-circles. Increasing the aspect ratio results in a transition from a flow field with a single +1 defect to flow fields hosting two vortices either separated by a +1 defect or two −1/2 defects. Each simulation has been repeated 50 times. As shown in **b**, the error bars correspond to the 95% confidence interval. **d**, Steady states where the right-most (v_2) and left-most (v_1) flows are parallel and prevail in boxes with large aspect ratios. The transition from antiferromagnetic to ferromagnetic contacts are not specific to colloidal rollers but generic to flocking matter (Toner–Tu fluids). **e**, Close-up view of the experimental streamlines measured in a channel where $\epsilon < \epsilon^*$. The green arrow indicates the local orientation of the flows. The antiferromagnetic couplings between adjacent streamlines promote crumpled and segregated streamlines. **f**, Same data as in **e**, but for $\epsilon > \epsilon^*$. The ferromagnetic couplings promote persistent and nested streamlines.

We are now equipped to state the laws of active hydraulics in trivalent networks and map them on a double-spin model. This mapping will allow us to predict the self-similar geometry of the streamlines, their gyration radius, degree of nesting and pair correlation. The four laws are as follows.

(i) The fluid activity constrains the current Φ_{ij} on the edge $e = (i, j)$ to take only three different values, namely, $\Phi_{ij}/\Phi_0 \in \{-1, 0, +1\}$.

(ii) In straight channels, the stability of laminar active flows penalizes the state where $\Phi_{ij} = 0$.

(iii) At every node i, mass conservation imposes the spin-ice constraint: $\sum_j \Phi_{ij} = 0$. This constraint frustrates the law stated in (ii).

(iv) The topological defects of the flow field in channels hosting no net current impose effective ferromagnetic, or antiferromagnetic, interactions between adjacent streamlines. The sign of the interactions is set by the channel aspect ratio.

The first three laws above define the spin-ice rules shown in Fig. 2c and are akin to the AFN model discussed elsewhere[14,15,17]. They must be complemented by the law in (iv) above to explain the polymorphism of streamlines observed in all our experiments and quantified in Fig. 3.

We now build a model to quantitatively account for these four elementary laws. To do so, we introduce an effective Hamiltonian $\mathcal{H}$ that couples two classical spin-1 variables. The edge spins $\Phi_{ij} = \pm 1, 0$ model the local fluxes, and the node spins $\sigma_i = \pm 1, 0$ encode the

handedness of the ith node (Fig. 2c). This Hamiltonian takes the compact form:

$$\mathcal{H} = -J_A \sum_{(i,j)} \Phi_{ij}^2 - J_C \sum_{(i,j)} \delta_{\Phi_{ij},0}\sigma_i\sigma_j, \tag{1}$$

where both sums are taken over the edges of the network. The first term reflects the activity of the fluid. J_A is a positive constant that penalizes the states of vanishing flows (law (ii) above). The second term reflects the interactions between adjacent streamlines (law (iv)) and J_C is a proxy for the channel aspect ratio. $J_C < 0$ corresponds to antiferromagnetic couplings, that is, channels where $\epsilon < \epsilon^*$. $J_C > 0$ corresponds to ferromagnetic couplings, that is, channels where $\epsilon > \epsilon^*$ (Fig. 4a,e,f). We stress that J_C only couples nodes connected by channels where the flux vanishes. This property is accounted for by the $\delta_{\Phi_{ij},0}$ term. The geometry and handedness of the streamline loops map on the ensembles of connected edge spins in the states that minimize $\mathcal{H}$. To find these states, we note that the Φ_{ij} and σ_i variables are not independent and use a Monte Carlo worm algorithm[31] that samples only the Φ_{ij} configurations compatible with the mass-conservation constraint expressed by law (iii).

We compare our numerical and experimental findings in Fig. 3b. The excellent agreement between the computed and measured

structural properties confirms the predictive power of our active hydraulic laws.

We can now gain a deeper insight by investigating three asymptotic limits: $J_C \gg 0$ (strong ferromagnetic interactions), $J_C \ll 0$ (strong antiferromagnetic interactions) and $J_C = 0$ (uncoupled streamlines). Remarkably, in the antiferromagnetic and non-interacting limits, quantitative analogies with a series of statistical field theories allow us to predict the exact scaling laws for the gyration radius and pair correlation functions of the streamline patterns.

Strong ferromagnetic interactions, namely, trivalent networks of long channels

This geometry, which corresponds to $\epsilon > \epsilon^*$, is modelled by Hamiltonians where $J_C \gg 0$. They are the most difficult to analyse. This difficulty stems from the subextensive degeneracy of the ground states. This observation was first made on the three-colouring model[32], which maps on equation (1) (Supplementary Information and Fig. 2b). The ground-state configurations of $\mathcal{H}$ indeed correspond to patterns of edge spins that uniformly minimize the ferromagnetic interactions. Back to the active hydraulic problem, we expect the ferromagnetic interaction to be minimized by fully nested streamlines. We never observe such configurations, neither in our experiments nor in our simulations. The reason is that we only probe metastable states of nested clusters (Fig. 3a), for which no exact prediction is currently available. We, however, fully characterize the geometry of the metastable states in finite-size systems (Supplementary Information). Despite their non-universal nature, Fig. 3b shows that our model correctly accounts for the measured gyration radius and pair correlations.

Strong antiferromagnetic interactions, namely, trivalent networks of short channels

In the limit of $\epsilon \ll \epsilon^*$, we can unambiguously define a net circulation around each face of the honeycomb lattice (Supplementary Fig. 9b). The handedness of the circulation around each face defines yet another classical spin variable, namely, $\Omega = \pm 1$, which measures the local height h of the topographic map (Fig. 3a,b): $\Omega = 2|h| - 1$. Altogether, the constraints imposed by strong activity ($J_A \gg 0$) and strong antiferromagnetic interactions ($J_C \ll 0$) translate into antiferromagnetic couplings between adjacent Ω spins. As a result, in this regime, the streamlines are nothing else but the domain walls between regions of opposite magnetization in the ground states of a frustrated Ising antiferromagnet (Supplementary Fig. 9b). We use this equivalence to exactly compute the nesting level Δh, gyration radius exponent ν and the pair correlation function $C(r)$, that is, the probability to find two edges at a distance r in the same loop (Fig. 3b). The domain walls of the Ising antiferromagnet are obviously segregated and the nesting level is given by $\Delta h = 1$ (ref. 32). The exact predictions of the gyration radius exponent and the decay of $C(r)$ are more complex to compute. They rely on the mapping of antiferromagnetic Ising models on the loop $O(1)$ theory[33] (Supplementary Information). Using this mapping, we find $\nu = 4/7$ (refs. 34,35) and $C(r) \approx r^{-1/2}$. These three exact predictions agree with our experimental findings and numerical simulations in the limit $\epsilon < \epsilon^*$ ($J_C \ll 0$) (Fig. 3b and Supplementary Information).

Vanishing edge-spin interactions, namely, uncoupled streamlines

Finally, when the coupling between adjacent edge spins vanishes ($J_C = 0$), our model reduces to Baxter's three-colouring model[24]. It consists of colouring the edges of a honeycomb lattice (Fig. 2c). Baxter's model maps on an exactly solvable statistical model of interacting loops known as the loop $O(2)$ model (Supplementary Information). The loops of this model identify to the streamlines of the active fluid. Using this second powerful analogy, we find that the gyration radius exponent should be $\nu_0 = 2/3$ (ref. 35), and that $C(r) \approx r^{-1}$. Remarkably,

these two exact predictions agree with the values measured in our experiments and simulations at the crossover between the ferromagnetic and antiferromagnetic regimes (Fig. 3c).

Altogether, the agreement between our experiments and theories establish the predictive power of our spin model, which accurately describes the random geometry of frustrated active hydraulics flows.

As a final remark, we stress that the four local laws of active hydraulics apply broadly, beyond the specifics of periodic lattices and polar active matter. They should describe the flows of any form of active fluid animated by spontaneous laminar flows in complex trivalent networks, from cell tissues to bacteria suspensions to active gels and liquid crystals.

We, therefore, expect our findings to provide a robust set of design rules for active microfluidic devices and offer new insights into the dynamics of groups of living cells and animals in heterogeneous environments and complex habitats[36–38].

Online content

Any methods, additional references, Nature Portfolio reporting summaries, source data, extended data, supplementary information, acknowledgements, peer review information; details of author contributions and competing interests; and statements of data and code availability are available at https://doi.org/10.1038/s41567-023-02301-2.

References

1. Rost, S. *Irrigation in Early States: New Directions* (The Oriental Institute, 2022).
2. Hagen, G. Ueber die bewegung des wassers in engen cylindrischen röhren. *Ann. Phys.* **122**, 423–442 (1839).
3. Poiseuille, J. L. *Recherches expérimentales sur le mouvement des liquides dans les tubes de très-petits diamètres* (Imprimerie Royale, 1844).
4. Darcy, H. *Les fontaines publiques de la ville de Dijon: exposition et application des principes à suivre et des formules à employer dans les questions de distribution d'eau* Vol. 2 (Victor Dalmont, 1856).
5. Marchetti, M. C. et al. Hydrodynamics of soft active matter. *Rev. Mod. Phys.* **85**, 1143–1189 (2013).
6. Bricard, A., Caussin, J.-B., Desreumaux, N., Dauchot, O. & Bartolo, D. Emergence of macroscopic directed motion in populations of motile colloids. *Nature* **503**, 95–98 (2013).
7. Wioland, H., Lushi, E. & Goldstein, R. E. Directed collective motion of bacteria under channel confinement. *New J. Phys.* **18**, 075002 (2016).
8. Zhang, J., Luijten, E., Grzybowski, B. A. & Granick, S. Active colloids with collective mobility status and research opportunities. *Chem. Soc. Rev.* **46**, 5551–5569 (2017).
9. Wu, K.-T. et al. Transition from turbulent to coherent flows in confined three-dimensional active fluids. *Science* **355**, eaal1979 (2017).
10. Doostmohammadi, A., Ignés-Mullol, J., Yeomans, J. M. & Sagués, F. Active nematics. *Nat. Commun.* **9**, 3246 (2018).
11. Saintillan, D. Rheology of active fluids. *Annu. Rev. Fluid Mech.* **50**, 563–592 (2018).
12. Opathalage, A. et al. Self-organized dynamics and the transition to turbulence of confined active nematics. *Proc. Natl Acad. Sci. USA* **116**, 4788–4797 (2019).
13. Morin, A. & Bartolo, D. Flowing active liquids in a pipe: hysteretic response of polar flocks to external fields. *Phys. Rev. X* **8**, 021037 (2018).
14. Woodhouse, F. G. & Dunkel, J. Active matter logic for autonomous microfluidics. *Nat. Commun.* **8**, 15169 (2017).
15. Woodhouse, F. G., Forrow, A., Fawcett, J. B. & Dunkel, J. Stochastic cycle selection in active flow networks. *Proc. Natl Acad. Sci. USA* **113**, 8200–8205 (2016).

16. Forrow, A., Woodhouse, F. G. & Dunkel, J. Mode selection in compressible active flow networks. *Phys. Rev. Lett.* **119**, 028102 (2017).
17. Woodhouse, F. G., Fawcett, J. B. & Dunkel, J. Information transmission and signal permutation in active flow networks. *New J. Phys.* **20**, 035003 (2018).
18. Hardoüin, J., Laurent, J., Lopez-Leon, T., Ignés-Mullol, J. & Sagués, F. Active microfluidic transport in two-dimensional handlebodies. *Soft Matter* **16**, 9230–9241 (2020).
19. Moessner, R. & Ramirez, A. P. Geometrical frustration. *Phys. Today* **59**, 24–29 (2006).
20. Nisoli, C., Moessner, R. & Schiffer, P. Colloquium: artificial spin ice: designing and imaging magnetic frustration. *Rev. Mod. Phys.* **85**, 1473–1490 (2013).
21. Ortiz-Ambriz, A., Nisoli, C., Reichhardt, C., Reichhardt, C. J. & Tierno, P. Colloquium: ice rule and emergent frustration in particle ice and beyond. *Rev. Mod. Phys.* **91**, 041003 (2019).
22. Udagawa, M. & Jaubert, L. (eds) *Spin Ice* (Springer International Publishing, 2021).
23. Wioland, H., Woodhouse, F. G., Dunkel, J. & Goldstein, R. E. Ferromagnetic and antiferromagnetic order in bacterial vortex lattices. *Nat. Phys.* **12**, 341–345 (2016).
24. Baxter, R. J. Colorings of a hexagonal lattice. *J. Math. Phys.* **11**, 784–789 (1970).
25. Baxter, R. J. *Exactly Solved Models in Statistical Mechanics* (Elsevier, 2016).
26. Nienhuis, B. Exact critical point and critical exponents of $O(n)$ models in two dimensions. *Phys. Rev. Lett.* **49**, 1062–1065 (1982).
27. Toner, J. & Tu, Y. Long-range order in a two-dimensional dynamical *XY* Model: how birds fly together. *Phys. Rev. Lett.* **75**, 4326–4329 (1995).
28. Toner, J. & Tu, Y. Flocks, herds, and schools: a quantitative theory of flocking. *Phys. Rev. E* **58**, 4828–4858 (1998).
29. Geyer, D., Martin, D., Tailleur, J. & Bartolo, D. Freezing a flock: motility-induced phase separation in polar active liquids. *Phys. Rev. X* **9**, 031043 (2019).
30. Chardac, A., Hoffmann, L. A., Poupart, Y., Giomi, L. & Bartolo, D. Topology-driven ordering of flocking matter. *Phys. Rev. X* **11**, 031069 (2021).
31. Barkema, G. T. & Newman, M. E. J. Monte Carlo simulation of ice models. *Phys. Rev. E* **57**, 1155–1166 (1998).
32. Verpoort, P. C., Simmons, J. & Castelnovo, C. Color-dependent interactions in the three coloring model. *Phys. Rev. B* **98**, 024403 (2018).
33. Blöte, H. W. J. & Nienhuis, B. Fully packed loop model on the honeycomb lattice. *Phys. Rev. Lett.* **72**, 1372–1375 (1994).
34. Kondev, J. & Henley, C. L. Geometrical exponents of contour loops on random Gaussian surfaces. *Phys. Rev. Lett.* **74**, 4580–4583 (1995).
35. Kondev, J., de Gier, J. & Nienhuis, B. Operator spectrum and exact exponents of the fully packed loop model. *J. Phys. A: Math. Gen.* **29**, 6489–6504 (1996).
36. Hansell, M. *Animal Architecture* (Oxford Univ. Press, 2005).
37. Perna, A. & Theraulaz, G. When social behaviour is moulded in clay: on growth and form of social insect nests. *J. Exp. Biol.* **220**, 83–91 (2017).
38. Martinez-Calvo, A., Trenado-Yuste, C. & Datta, S. in *Out-of-equilibrium Soft Matter: Active Fluids* (eds Kurzthaler, C. et al.) Ch. 5 (Royal Society of Chemistry, 2023).

Methods

Quincke roller fluids

The experimental setup is described elsewhere[39,40]. In short, we use polystyrene colloids with a radius of 2.4 μm (Thermo Scientific G0500) dispersed in a solution of hexadecane including 5.5×10^{-2} wt% of dioctyl sulfosuccinate sodium salt. The microfluidic devices are made of two electrodes spaced by a 25-μm-thick double-sided tape. We pattern the bottom surface of the device with channel networks. They are made of a 2-μm-thick layer of insulating photoresist resin (Microposit S1818) patterned by means of standard ultraviolet lithography[39]. In all our experiments, the networks have the shape of a honeycomb structure. The width of the channels is 200 μm and we vary their lengths from 120 to 220 μm. The overall size of the channel network is in the order of 1.5×1.5 cm^2.

The electrodes are glass slides coated with indium tin oxide (Solems, ITOSOL30; thickness, 80 nm). We start the experiments by homogeneously filling the microfluidic chambers with the colloidal solution. Then, we let the colloids sediment on the bottom electrode. The average packing fraction of the colloidal monolayer is approximately equal to 30% in all our experiments. We operate at this packing fraction to make sure that our active fluid remains in the polar liquid state, far from the flocking-transition threshold. Within our experimental conditions, homogeneous polar fluids form when the packing fraction exceeds ~10% (ref. 6). We then apply a d.c. voltage of 110 V to trigger the Quincke instability and cause the colloids to roll at a constant speed of $v_0 \approx 0.8$ mm s^{-1} on the bottom electrode. Each experiment is repeated from six to ten times.

Measurement of velocity fields

Once the active flow reaches a steady state, we image the whole network for 5 s with a Nikon AZ100 microscope. We record the videos with a Luxima LUX160 camera (Ximea) at a frame rate of 200 fps. To measure the velocity field **v**, we use a conventional particle imaging velocimetry (PIV) instrument. In practice, we use the PIVlab MATLAB R2019b package[41]. The PIV box size is 48×48 μm^2, and the PIV boxes overlap over a half of their size (Extended Data Fig. 3a,b). In all our measurements, we find that the boundary condition of the velocity field close to the confining wall of the channels is a full-slip condition, in agreement with all the previous experiments on colloidal roller fluids.

Before constructing the streamlines, we average the velocity field over the width of each channel (Extended Data Fig. 3). We define the average velocity in each channel as a scalar quantity. We use the bipartite geometry of the honeycomb lattice to define its sign. Our sign convention is more easily explained using the sketch shown in Extended Data Fig. 3c. Denoting the two sublattices by 'a' and 'b' in this figure, we choose to assign a '+' sign (blue colour) to the velocity when the fluid flows from the a node to the b node and a '−' sign (orange colour) when the fluid flows from the b node to the a node.

Density and current fields

To measure the local current fields $\mathbf{j}(\mathbf{r}) \equiv \rho(\mathbf{r})\mathbf{v}(\mathbf{r})$, we measure the density and velocity field in two different videos of the same experiment. For both measurements, we use a Hamamatsu ORCA-Quest qCMOS camera mounted on a Nikon AZ100 microscope with a ×2 objective. As we cannot image the whole network at once, we perform multiple acquisitions and stitch our images, which is always possible in the steady state. To measure the density field, we perform epifluorescence imaging at 10 fps, and use the local fluorescence intensity as a proxy for the colloid density. Extended Data Fig. 4a shows that, as expected, both quantities are proportional to one another. The calibration was performed on static images using a higher magnification and using a conventional particle detection algorithm (ImageJ 1.52a).

We then use bright-field imaging and record at a higher frame rate (200 fps) to perform our PIV analysis. The PIV box size is 24×24 μm^2. We then average both density ρ and velocity fields **v** over time and we multiply them to reconstruct the local current field **j** (Extended Data Fig. 4b–d). Finally, we measure the average current Φ_{ij} along the edges of the network by averaging **j** over the channel joining nodes i and j.

Construction of streamlines

In this section, we detail how we analyse our data. We use the same methods and algorithms for our experimental and numerical data.

To construct the streamlines, we first define a discrete current field Φ_e on edge e connecting the nodes i and j. Φ_e can take three different values: ±1 in channels that support a net current and 0 in channel hosting vortices. In practice, we construct the Φ_e field as follows. We measure the average scalar product between the local velocity and unit vector pointing in the direction of a channel. The average is performed over the channel area. When this quantity is larger than 0.5, we set $\Phi_e = +1$; when it is smaller than −0.5, we set $\Phi_e = -1$, and $\Phi_e = 0$ otherwise. In our simulations $\Phi = \pm1$, 0 by definition.

Once the Φ_e values are defined, we can unambiguously construct the oriented streamlines along the principal axis of the honeycomb lattice. We then use a depth-first search algorithm to detect and label each individual loop in the streamlines soup[42].

Once the individual loops are identified, we can readily measure their gyration radius and the probability $C(r)$ that two edges of the lattice separated by distance r belong to the same loop (Supplementary Section IV.B).

Constructing a topographic map from an ensemble of oriented streamlines

We now explain how to quantify the nesting of streamlines. To do so, we first convert the ensemble of oriented loops into a topographic map. We denote $\mathcal{F}$ as the ensemble of hexagonal faces of the honeycomb network. Considering a configuration $\{\Phi_e\}$ of the current field on the edges, we define a height field h_f on the faces.

Once the loops are oriented, we can define the winding number of each loop around a given face f: it is equal to ±1 when the face is lassoed by the loop, and 0 otherwise. The height field of the topographic map is then defined at a face of the network as the sum of the winding numbers of all the loops winding around this point. As a reference, the height is taken to be zero outside the network.

In practice, we recursively measure the height field h_f. The procedure is easily understood from the sketch of the algorithm shown in Extended Data Fig. 5a. In short, starting from face f associated with height h, we move to the neighbouring face f' by crossing an edge e. If e hosts a spin pointing towards the right-hand (left-hand) side, we assign the value $h' = h - 1$ ($h' = h + 1$). The right and left directions are defined with respect to the vector connecting the centres of f and f'. When the edge hosts no current ($\Phi_e = 0$), then $h' = h$. The resulting height field does not depend on the way the network is explored. This procedure is very similar to the standard mapping of loop $O(n)$ models to solid-on-solid models[26].

The reason why we introduce this mapping is twofold. First, the height amplitude $\Delta h = \max_{\mathcal{F}} h_f - \min_{\mathcal{F}} h_f$ is one of our key observables. It quantifies the nesting of the streamlines and distinguishes between the two phases observed in both experiments and simulations (Fig. 3 and Supplementary Section IV.B). Second, this mapping allows us to map the streamlines of the crumpled phase to the domain walls of the antiferromagnetic Ising model on the triangular lattice of faces $\mathcal{F}$ (Supplementary Section V.B).

Reporting summary

Further information on research design is available in the Nature Portfolio Reporting Summary linked to this article.

Data availability

All data supporting this study are available via Zenodo at https://doi.org/10.5281/zenodo.8426828. Source data are provided with this paper.

Code availability

All codes supporting this study are available via Zenodo at https://doi.org/10.5281/zenodo.8426828.

References

39. Morin, A., Desreumaux, N., Caussin, J.-B. & Bartolo, D. Distortion and destruction of colloidal flocks in disordered environments. *Nat. Phys.* **13**, 63–67 (2017).
40. Geyer, D., Morin, A. & Bartolo, D. Sounds and hydrodynamics of polar active fluids. *Nat. Mater.* **17**, 789–793 (2018).
41. Thielicke, W. & Stamhuis, E. PIVlab—towards user-friendly, affordable and accurate digital particle image velocimetry in MATLAB. *J. Open Res. Softw.* **2**, 30 (2014).
42. Cormen, T. H., Leiserson, C. E., Rivest, R. L. & Stein, C. *Introduction to Algorithms* (MIT Press, 2022).

Author contributions

C.J., A.C. and A.P. have equally contributed to this work. D.B. designed the project. A.C. and C.J. performed the experiments. C.J. and A.P. performed the finite-element simulations. A.P. worked out the theory and performed the Monte Carlo simulations. All authors discussed the results and wrote the manuscript.

Competing interests

The authors declare no competing interests.

Additional information

Extended data is available for this paper at https://doi.org/10.1038/s41567-023-02301-2.

Supplementary information The online version contains supplementary material available at https://doi.org/10.1038/s41567-023-02301-2.

**Correspondence and requests for materials** should be addressed to Denis Bartolo.

Peer review information *Nature Physics* thanks the anonymous reviewers for their contribution to the peer review of this work.

Reprints and permissions information is available at www.nature.com/reprints.
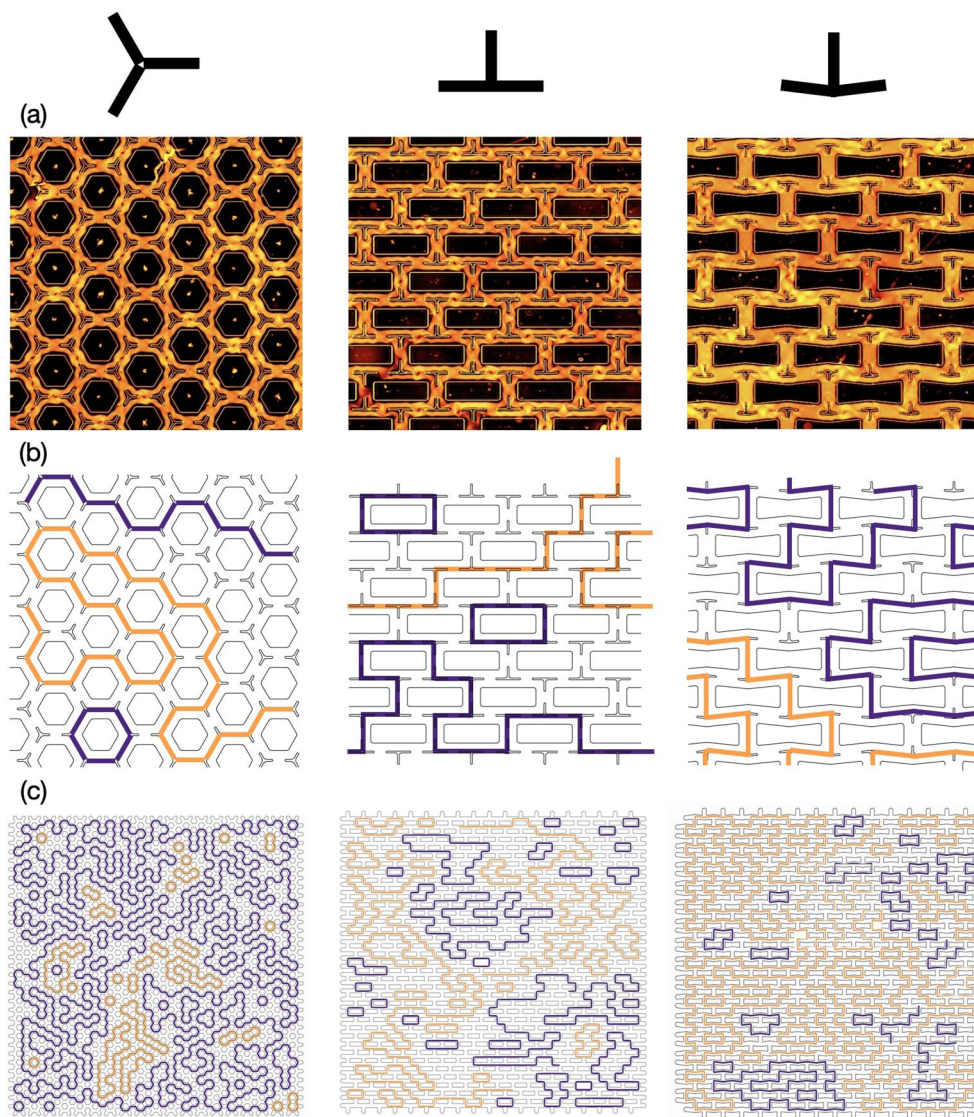
Extended Data Fig. 1 | Streamline geometries in three trivalent network geometries. To better establish the robustness of our findings we have conducted experiments in three types of periodic trivalent networks. They all correspond to continuous deformations of the honeycomb geometry. **(a)** Pictures of the three experiments conducted in three different networks. The channel width is the same in the three experiments (200 μm). **(b)** Close-up on the streamlines corresponding to the region of the network shown in (a). **(c)** Full geometry of the streamlines. In all three cases they form self-avoiding loops, and the fraction of nodes where the three currents vanish is subdominant but depend on the specific geometry of the nodes. We note that in the brick wall geometry we find some interrupted streamlines due to defects in the design that cause local density fluctuations.
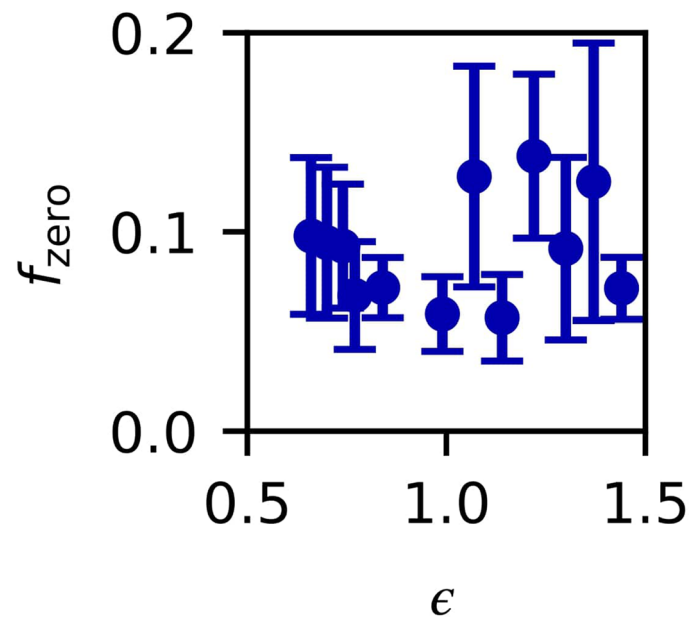
Extended Data Fig. 2 | Fraction of nodes with three vanishing fluxes. The fraction f_{zero} does not change significantly with ϵ and remains around 0.1. The error bars correspond to the 95% confidence interval.
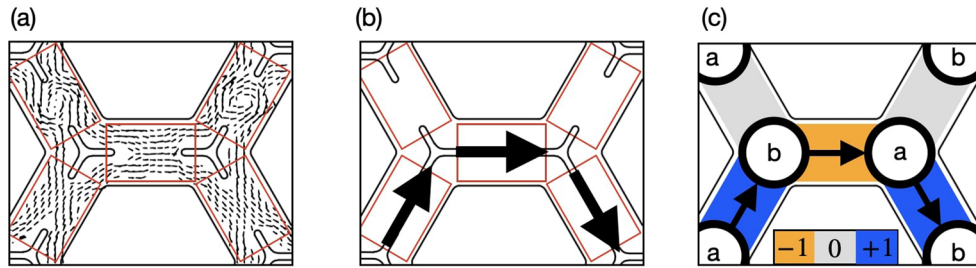
Extended Data Fig. 3 | From local velocity fields to streamlines and three-coloring models. (a) Velocity field. The averaging windows are sketched in red. **(b)** Sketch of the averaged velocity in each averaging window. **(c)** Scalar value of the velocity. It is + 1 (resp. − 1) when the fluid flows on average from a 'a'-node to a 'b'-node (resp. from a 'b'-node node to a 'a'-node).
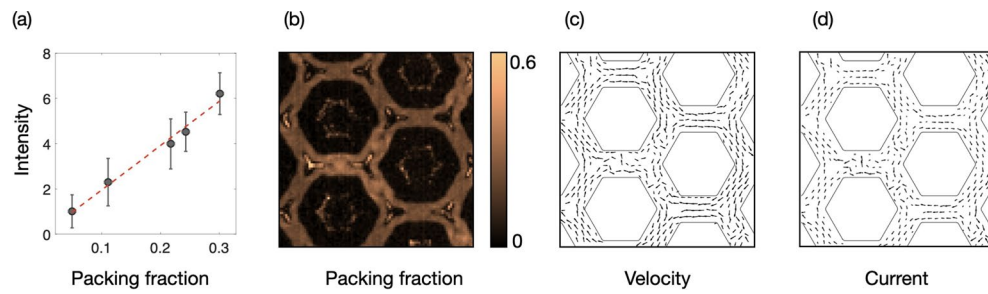
Extended Data Fig. 4 | Measuring the local density and current fields at the subchannel scale. (a) Fluorescence intensity plotted against to the packing fraction ρ. **(b)** Colormap of the packing fraction field. **(c)** Velocity field. **(d)** Current field computed from (b) and (c).
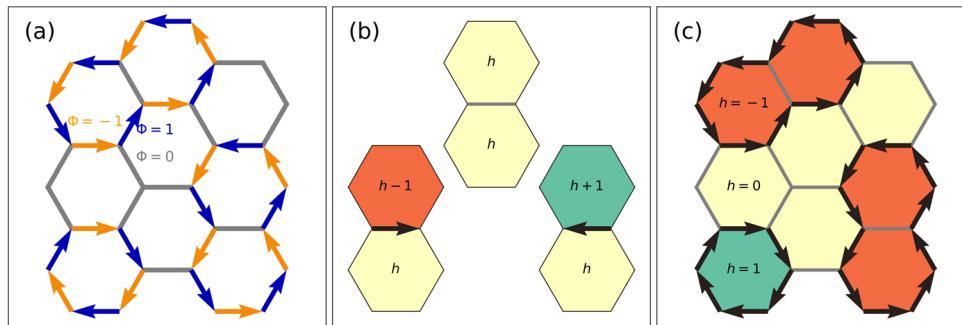
Extended Data Fig. 5 | Mapping of the streamlines on a topographic map.
(a) Configuration of our model (see Fig. 2b). **(b)** Rules for the topographic map. If the edge is gray, If there is no arrow, the two faces have the same height. If there is an arrow pointing to the right, when moving from f to f', then $h_{f'} = h_f - 1$. If there is an arrow to the left, then $h_{f'} = h_f + 1$. **(c)** Topographic map corresponding to (a). In this configuration, $\Delta h = \max h - \min h = 2$.

Corresponding author(s): Denis Bartolo

Last updated by author(s): Camille Jorge

Reporting Summary

Nature Portfolio wishes to improve the reproducibility of the work that we publish. This form provides structure for consistency and transparency in reporting. For further information on Nature Portfolio policies, see our Editorial Policies and the Editorial Policy Checklist.

Please do not complete any field with "not applicable" or n/a. Refer to the help text for what text to use if an item is not relevant to your study.
For final submission: please carefully check your responses for accuracy; you will not be able to make changes later.

Statistics

For all statistical analyses, confirm that the following items are present in the figure legend, table legend, main text, or Methods section.

n/a	Confirmed	
☐	☑	The exact sample size (*n*) for each experimental group/condition, given as a discrete number and unit of measurement
☐	☑	A statement on whether measurements were taken from distinct samples or whether the same sample was measured repeatedly
☑	☐	The statistical test(s) used AND whether they are one- or two-sided *Only common tests should be described solely by name; describe more complex techniques in the Methods section.*
☑	☐	A description of all covariates tested
☑	☐	A description of any assumptions or corrections, such as tests of normality and adjustment for multiple comparisons
☐	☑	A full description of the statistical parameters including central tendency (e.g. means) or other basic estimates (e.g. regression coefficient) AND variation (e.g. standard deviation) or associated estimates of uncertainty (e.g. confidence intervals)
☑	☐	For null hypothesis testing, the test statistic (e.g. F, t, r) with confidence intervals, effect sizes, degrees of freedom and P value noted *Give P values as exact values whenever suitable.*
☑	☐	For Bayesian analysis, information on the choice of priors and Markov chain Monte Carlo settings
☑	☐	For hierarchical and complex designs, identification of the appropriate level for tests and full reporting of outcomes
☑	☐	Estimates of effect sizes (e.g. Cohen's *d*, Pearson's *r*), indicating how they were calculated

Our web collection on statistics for biologists contains articles on many of the points above.

Software and code

Policy information about availability of computer code

Data collection	https://doi.org/10.5281/zenodo.8426828
Data analysis	https://doi.org/10.5281/zenodo.8426828

For manuscripts utilizing custom algorithms or software that are central to the research but not yet described in published literature, software must be made available to editors and reviewers. We strongly encourage code deposition in a community repository (e.g. GitHub). See the Nature Portfolio guidelines for submitting code & software for further information.

Data

Policy information about availability of data

All manuscripts must include a data availability statement. This statement should provide the following information, where applicable:
- Accession codes, unique identifiers, or web links for publicly available datasets
- A description of any restrictions on data availability
- For clinical datasets or third party data, please ensure that the statement adheres to our policy

Il data supporting this study are available on the public repository https://doi.org/10.5281/zenodo.8426828.

Research involving human participants, their data, or biological material

Policy information about studies with human participants or human data. See also policy information about sex, gender (identity/presentation), and sexual orientation and race, ethnicity and racism.

Reporting on sex and gender	n/a
Reporting on race, ethnicity, or other socially relevant groupings	n/a
Population characteristics	n/a
Recruitment	n/a
Ethics oversight	n/a

Note that full information on the approval of the study protocol must also be provided in the manuscript.

Field-specific reporting

Please select the one below that is the best fit for your research. If you are not sure, read the appropriate sections before making your selection.

☐ Life sciences   ☐ Behavioural & social sciences   ☐ Ecological, evolutionary & environmental sciences

For a reference copy of the document with all sections, see nature.com/documents/nr-reporting-summary-flat.pdf

Life sciences study design

All studies must disclose on these points even when the disclosure is negative.

Sample size	
Data exclusions	
Replication	
Randomization	
Blinding	

Behavioural & social sciences study design

All studies must disclose on these points even when the disclosure is negative.

Study description	
Research sample	
Sampling strategy	
Data collection	
Timing	
Data exclusions	
Non-participation	
Randomization	

Ecological, evolutionary & environmental sciences study design

All studies must disclose on these points even when the disclosure is negative.

Study description	
Research sample	
Sampling strategy	
Data collection	
Timing and spatial scale	
Data exclusions	
Reproducibility	
Randomization	
Blinding	

Did the study involve field work? ☐ Yes ☐ No

Field work, collection and transport

Field conditions	
Location	
Access & import/export	
Disturbance	

Reporting for specific materials, systems and methods

We require information from authors about some types of materials, experimental systems and methods used in many studies. Here, indicate whether each material, system or method listed is relevant to your study. If you are not sure if a list item applies to your research, read the appropriate section before selecting a response.

Materials & experimental systems

n/a	Involved in the study
☑	☐ Antibodies
☑	☐ Eukaryotic cell lines
☑	☐ Palaeontology and archaeology
☑	☐ Animals and other organisms
☑	☐ Clinical data
☑	☐ Dual use research of concern
☑	☐ Plants

Methods

n/a	Involved in the study
☑	☐ ChIP-seq
☑	☐ Flow cytometry
☑	☐ MRI-based neuroimaging

Antibodies

Antibodies used	
Validation	

Eukaryotic cell lines

Policy information about cell lines and Sex and Gender in Research

Cell line source(s)	
Authentication	
Mycoplasma contamination	
Commonly misidentified lines (See ICLAC register)	

Palaeontology and Archaeology

Specimen provenance	
Specimen deposition	
Dating methods	

☐ Tick this box to confirm that the raw and calibrated dates are available in the paper or in Supplementary Information.

Ethics oversight	

Note that full information on the approval of the study protocol must also be provided in the manuscript.

Animals and other research organisms

Policy information about studies involving animals; ARRIVE guidelines recommended for reporting animal research, and Sex and Gender in Research

Laboratory animals	
Wild animals	
Reporting on sex	
Field-collected samples	
Ethics oversight	

Note that full information on the approval of the study protocol must also be provided in the manuscript.

Clinical data

Policy information about clinical studies

All manuscripts should comply with the ICMJE guidelines for publication of clinical research and a completed CONSORT checklist must be included with all submissions.

Clinical trial registration	
Study protocol	
Data collection	
Outcomes	

Dual use research of concern

Policy information about dual use research of concern

Hazards

Could the accidental, deliberate or reckless misuse of agents or technologies generated in the work, or the application of information presented in the manuscript, pose a threat to:

No	Yes	
v	☐	Public health
v	☐	National security
v	☐	Crops and/or livestock
v	☐	Ecosystems
v	☐	Any other significant area

Experiments of concern

Does the work involve any of these experiments of concern:

No	Yes	
v	☐	Demonstrate how to render a vaccine ineffective
v	☐	Confer resistance to therapeutically useful antibiotics or antiviral agents
v	☐	Enhance the virulence of a pathogen or render a nonpathogen virulent
v	☐	Increase transmissibility of a pathogen
v	☐	Alter the host range of a pathogen
v	☐	Enable evasion of diagnostic/detection modalities
v	☐	Enable the weaponization of a biological agent or toxin
v	☐	Any other potentially harmful combination of experiments and agents

Plants

Seed stocks	
Novel plant genotypes	
Authentication	

ChIP-seq

Data deposition

☐ Confirm that both raw and final processed data have been deposited in a public database such as GEO.

☐ Confirm that you have deposited or provided access to graph files (e.g. BED files) for the called peaks.

Data access links *May remain private before publication.*	
Files in database submission	
Genome browser session (e.g. UCSC)	

Methodology

Replicates	
Sequencing depth	
Antibodies	
Peak calling parameters	
Data quality	
Software	

Flow Cytometry

Plots

Confirm that:

☐ The axis labels state the marker and fluorochrome used (e.g. CD4-FITC).

☐ The axis scales are clearly visible. Include numbers along axes only for bottom left plot of group (a 'group' is an analysis of identical markers).

☐ All plots are contour plots with outliers or pseudocolor plots.

☐ A numerical value for number of cells or percentage (with statistics) is provided.

Methodology

Sample preparation

Instrument

Software

Cell population abundance

Gating strategy

☐ Tick this box to confirm that a figure exemplifying the gating strategy is provided in the Supplementary Information.

Magnetic resonance imaging

Experimental design

Design type

Design specifications

Behavioral performance measures

Imaging type(s)

Field strength

Sequence & imaging parameters

Area of acquisition

Diffusion MRI   ☐ Used   ☐ Not used

Preprocessing

Preprocessing software

Normalization

Normalization template

Noise and artifact removal

Volume censoring

Statistical modeling & inference

Model type and settings

Effect(s) tested

Specify type of analysis: ☐ Whole brain   ☐ ROI-based   ☐ Both

Statistic type for inference

(See [Eklund et al. 2016](#))

Correction

Models & analysis

n/a	Involved in the study
☐	☐ Functional and/or effective connectivity
☐	☐ Graph analysis
☐	☐ Multivariate modeling or predictive analysis

Functional and/or effective connectivity

Graph analysis

Multivariate modeling and predictive analysis